Chemical Reaction Networks Explain Gas Evolution Mechanisms in Mg-Ion Batteries

Evan Walter Clark Spotte-Smith,[†,‡] Samuel M. Blau,[¶] Daniel Barter,[¶] Noel J. Leon,[§] Nathan T. Hahn,[‖] Nikita S. Redkar,[⊥] Kevin R. Zavadil,[‖] Chen Liao,[*,§] and Kristin A. Persson[*,‡,#]

†*Materials Science Division, Lawrence Berkeley National Laboratory, 1 Cyclotron Road, Berkeley, CA, 94720 USA*

‡*Department of Materials Science and Engineering, University of California, Berkeley, 210 Hearst Memorial Mining Building, Berkeley, CA, 94720 USA*

¶*Energy Storage and Distributed Resources, Lawrence Berkeley National Laboratory, 1 Cyclotron Road, Berkeley, CA, 94720 USA*

§*Argonne National Laboratory, 9700 S. Cass Ave, Lemont, IL 60439 USA*

‖*Material, Physical and Chemical Sciences Center, Sandia National Laboratories, 1515 Eubank Blvd. SE, Albuquerque, NM 87123 USA*

⊥*Department of Chemical and Biomolecular Engineering, University of California, Berkeley, 201 Gilman Hall, Berkeley, CA, 94720 USA*

#*Molecular Foundry, Lawrence Berkeley National Laboratory, 1 Cyclotron Road, Berkeley, CA, 94720 USA*

E-mail: liaoc@anl.gov; kapersson@lbl.gov

Abstract

Out-of-equilibrium electrochemical reaction mechanisms are notoriously difficult to characterize. However, such reactions are critical for a range of technological applica-

tions. For instance, in metal-ion batteries, spontaneous electrolyte degradation controls electrode passivation and battery cycle life. Here, to improve on our ability to elucidate electrochemical reactivity, we combine computational chemical reaction network (CRN) analysis based on density functional theory (DFT) and differential electrochemical mass spectroscopy (DEMS) to study gas evolution from a model Mg-ion battery electrolyte — magnesium bistriflimide ($Mg(TFSI)_2$) dissolved in diglyme (G2). Automated CRN analysis allows for the facile interpretation of DEMS data, revealing H_2O, C_2H_4, and CH_3OH as major products of G2 decomposition. These findings are further explained by identifying elementary mechanisms using DFT. While $TFSI^-$ is reactive at Mg electrodes, we find that its decomposition does not meaningfully contribute to gas evolution. The combined theoretical-experimental approach developed here provides a means to elucidate electrolyte reactivity, improving our ability to predict decomposition products and pathways when initially unknown.

Introduction

Electrochemistry is increasingly applied to drive sustainable chemical and materials synthesis,[1,2] efficiently process wastewater,[3] and store renewable energy on the personal and the grid scale.[4,5] The design of electrochemical technologies in these and other areas requires a deep understanding of reactivity at electrified interfaces. Unfortunately, such understanding is notoriously elusive, particularly due to the essential role of complex, spontaneous cascade processes. There has been recent interest in applying high-throughput experimentation and machine learning to discover electrochemical reactions and predict reaction outcomes,[6,7] yet the identification of electrochemical reaction pathways and products remains challenging.[8] Electrochemical reaction mechanisms likewise cannot be easily analyzed by experiment,[9] in part because they are frequently driven by short-lived radical and ionic intermediates.[10]

Electrolyte degradation in metal-ion batteries is an example of a technologically important and highly complex electrochemical reaction cascade. In lithium-ion batteries (LIBs),

electrolytes decompose upon reduction to form solid electrolyte interphase (SEI) layers,[11,12] which enable reversible lithium transport to and from the electrode while limiting or eliminating further electron transport to the electrolyte.

In order to meet growing global demand for energy storage while mitigating resource scarcity as well geopolitical supply chain risk,[13,14] alternative battery technologies are needed. Magnesium-ion batteries (MIBs) present one such possible beyond-Li ion technology, alleviating some of the inherent limitations of current LIBs. However, the potential of MIBs is presently unrealized because of comparatively poor cycling behavior and unfavorable electrode passivation. Most electrolytes decompose at Mg negative electrodes during MIB charging. But rather than forming effective SEI layers as in LIBs, many MIB electrolytes degrade to produce ionically insulating films which prevent reversible Mg plating and stripping.[15,16] In fact, it was once widely believed that all electrolyte decomposition at Mg electrodes would lead to electrochemically inert films,[17] and the first instances of electrolytes decomposing to produce protective non-ionically-insulating SEI films on Mg were only discovered in the past ten years.[18–20]

Previous studies have provided relatively little detail regarding either reaction mechanisms or decomposition products involved in MIB electrolyte decomposition and interphase formation. In most cases where MIB interphases have been characterized,[18–24] the techniques used have identified simple inorganic components (e.g. MgO, MgS, or $MgCO_3$) or bonding motifs (e.g. C-O or C=O groups), unable to provide specific insight into organic speciation. Theoretical studies using density functional theory (DFT) and *ab initio* molecular dynamics (AIMD) can provide more detailed insight into electrolyte reactivity. However, previous DFT studies have primarily or exclusively considered the initial steps of electrolyte decomposition,[25–27] while AIMD is generally limited to extremely short time scales ($\sim$ 10ps) at idealized interfaces.[21,28]

In this work, we conduct a combined theoretical-experimental analysis to probe electrolyte degradation and gas evolution in a model MIB electrolyte — magnesium bistri-

flimide ($Mg(TFSI)_2$) dissolved in diglyme (G2). We perform online electrochemical mass spectroscopy (OEMS), a kind of differential electrochemical mass spectroscopy (DEMS), to detect gaseous byproducts of MIB electrolyte decomposition *in situ*. DEMS is a useful tool for instantaneous and quantitative detection of gaseous species evolved from solution during electrochemical testing,[29,30] and it has previously been used to quantitatively diagnose the gaseous species generated during lithium-ion battery cycling.[31–33] In order to explain and interpret OEMS data in MIBs, we computationally construct and analyze a chemical reaction network (CRN) describing electrolyte decomposition and SEI formation at the Mg plating potential. Using a recently developed method,[34] we automatically identify potential CRN products, as well as reaction pathways to form those products. With this information, we are able to positively identify the gases formed as byproducts of electrolyte decomposition. We then explain the presence of the observed gases by discovering and analyzing elementary reaction mechanisms for gas formation obtained using DFT. Our approach of combining CRN analysis with experimental spectroscopy provides a path forward for the in-depth analysis of chemical transformations in next-generation electrochemical systems with minimal prior knowledge.

Computational Methods

Species and Molecular Property Dataset

A dataset of species relevant to $Mg(TFSI)_2$/G2 electrolyte decomposition and interphase formation, the **MA**gnesium **D**ataset of **E**lectrolyte and **I**nterphase **R**e**A**gents (MADEIRA), was constructed using high-throughput DFT. The approach taken for the construction of this dataset was similar to that used to develop the Lithium-Ion Battery Electrolyte (LIBE) dataset reported previously.[35] Electrolyte species (including G2, $TFSI^-$, and related complexes with Mg ions) and known or suspected products were broken down into a set of fragment molecules. Due to limited experimental characterization, the products were limited to

inorganic species (e.g. $MgSO_3$) and small molecule gases (e.g. H_2). For each fragment, we obtained an optimized geometry, Gibbs free energy, and other properties (including atomic partial charges and atomic partial spin) using DFT with the ωB97X-V density functional,[36] def2-TZVPPD basis set,[37] and solvent model with density (SMD)[38] with solvent parameters for G2.[39] We denote this level of theory ωB97X-V/def2-TZVPPD/SMD(G2). Additional species were included based on selective recombination of the fragments. All calculations were conducted using the Q-Chem electronic structure code version 5,[40] and calculations were conducted in high throughput using the `atomate`[41] and `custodian`[42,43] libraries.

The complete dataset obtained using this procedure is available on Figshare.[44] We note that, because few products — and essentially no organic or polymeric products — of $Mg(TFSI)_2$/G2 electrolyte decomposition have been positively identified, we were not able to use knowledge of such products to improve the coverage of the dataset. As a result, the set of species obtained by this fragmentation-recombination procedure is almost certainly incomplete, with key species relevant to electrolyte decomposition and SEI formation likely missing. Work to expand this dataset is ongoing. We also note that we intend to describe this dataset in further detail in a future publication.

CRN Generation

Solvation Correction

While implicit solvation methods such as SMD are suitable for solution-phase calculations involving neutral and charged organic species, they severely underestimate the stabilizing effect of solvent on metal ions.[34]

To correct the (free) energies of species with undercoordinated Mg ions in our reaction network, we estimated the effect of each coordinate bond on the Mg^{2+} and Mg^{1+} ions. We optimized $Mg^{2+}(G_2)_n$ and $Mg^{1+}(G_2)_n$ clusters using DFT in Q-Chem, with $n \in \{0, 1, 2\}$. To lower the cost of these calculations, we optimized the clusters at the ωB97X-D/def2-SVPD/PCM[37,45,46] ($\varepsilon = 7.23$) level of theory, with single-point energy corrections performed

at the ωB97X-V/def2-TZVPPD/SMD(G2) level of theory as described above. We found (Supporting Information Figure S13) that each Mg-O coordinate bond stabilized Mg^{2+} by 1.37 eV, while Mg^{1+} was stabilized by 0.49 eV for each coordinate bond. In network construction, these values were modified slightly to 1.49 and 0.56 eV, respectively, in order to make expected coordination reactions slightly exergonic.

If any Mg ions are undercoordinated, then the free energy is lowered by the correction factors for each "missing" coordinate bond. We use partial charges obtained from Natural Bonding Orbital (NBO) version 5.0[47] analysis to determine the charge state of each Mg ion in order to apply the appropriate correction. When determining the number of "missing coordinate bonds", we assume that Mg^{2+} generally prefers a 6-fold coordination and Mg^{1+} prefers a 5-fold coordination.

As in our previous study,[34] when calculating reaction free energies for oxidation or reduction reactions, we used an uncorrected free energy. This is especially important for reduction reactions involving Mg due to the different preferred coordination environments of Mg^{2+} and Mg^{1+}. In addition, we do not apply a solvation correction when calculating energy barriers. The assumptions implicit in performing a correction for metal-ion solvation — namely, that the ion is always in an equilibrium solvation structure — break down when considering transition-states, which are inherently non-equilibrium structures.

Species Filtering

We used the High-Performance Reaction Generation (HiPRGen) method[34] to automatically construct CRNs from an initial set of species and their properties. HiPRGen is designed for cases where potential energy surface (PES) exploration techniques (stochastic surface walking,[48] AIMD, etc.) are too expensive to thoroughly capture the reactivity of a system and where reaction patterns are not sufficiently well understood to allow the use of prescriptive reaction templates. HiPRGen has previously been used to construct and analyze CRNs relevant to electrolyte degradation and SEI formation in LIBs.[34,49]

Instead of using PES exploration or templates, HiPRGen constructs CRNs using extensible filters. For this work, the following types of species were excluded:

- Molecules containing neutral or negative metal ions, where the charges are calculating by applying NBO to a single-point energy calculation at the ωB97X-V/def2-TZVPPD/SMD(G2) level of theory.
- Molecules composed of two or more disconnected fragments
- Metal-centric complexes, where two or more non-metal fragments are connected only by coordinate bonds to Mg ions
- Molecules with charge less than -2 or greater than 2

In addition to these filters, we ensure that there are no redundant species. That is, if there exist multiple molecules with the same charge, spin multiplicity, and structure (neglecting coordinate bonds with metal ions), we include only the molecule with the lowest solvation-corrected free energy. Using these filters, an initial set of 11,502 species was reduced to 6,469 species.

Reaction Filtering

After the species have been filtered, HiPRGen enumerates all possible stoichiometrically valid unimolecular or bimolecular reactions between these species. Because we are interested in electrochemical processes, where the electrolyte system is open to electrons, these stoichiometrically valid reactions conserve mass but do not necessarily conserve charge. Then, the stoichiometrically valid reactions are filtered in much the same way as the species are filtered. For this work, we used the same set of reaction filters that we have previously reported.[34] As some examples, we remove:

- Endergonic reactions with $\Delta G > 0$ eV.
- Reduction or oxidation reactions involving more than one electron ($|\Delta q| > 1$)

- Reactions involving spectators that do not directly participate
- Reactions involving more than two covalent bonds changing simultaneously

In total, we obtained 92,812,997 unique reactions using this filtering procedure.

Identification of CRN Products

We employed the Gillespie algorithm,[50,51] a stochastic method, to sample the reactive space defined by the HiPRGen-generated CRN. In order to explore as many diverse reaction pathways as possible, we conducted simulations with various initial states:

- 30 Mg^{2+}, 30 G2, and 30 $TFSI^-$
- 30 Mg^{2+}, 30 G2, 30 $TFSI^-$, and 30 CO_2
- 30 Mg^{2+}, 30 G2, 30 $TFSI^-$, and 30 OH^-
- 30 Mg^{2+}, 30 G2, 30 $TFSI^-$, 30 OH^-, and 30 $H^\bullet$
- 30 Mg^{2+}, 30 G2, 30 $TFSI^-$, 30 CO_2, 30 OH^-, and 30 $H^\bullet$

The choice to include 30 of each initial species is arbitrary and was determined empirically. Simulations involving too few molecules in the initial state will not allow many reactions to be sampled, while simulations involving many molecules will complete more slowly.

For each initial state, 50,000 trajectories of at most 250 steps were conducted. For each of the five sets of simulations, we obtained the stepwise average trajectories. The smoothing of the average trajectories (Supporting Information Figures S8-S12) indicates convergence to the exact expected behavior and confirms that we have sampled sufficiently. All simulations were conducted at the equilibrium potential of Mg (0V vs. Mg/Mg^{2+}).

Using the average trajectories, we automatically identified the CRN products. These CRN products are not necessarily the products of the corresponding real chemical system, but we have previously found[34] significant overlap between CRN products and experimentally

observed products in battery electrolyte systems. CRN products are defined using three heuristics previously described by Barter, Spotte-Smith, et al.[34] Specifically, a CRN product has a formation:consumption ratio of at least 1.5 (the species must be formed three times as a product of a reaction for every two times it is consumed as a reactant), has an average amount of at least 0.1 in the final state (at least one of the species remains at the end of every ten trajectories), and can be formed via a pathway with cost lower than 10, where the cost of a reaction is $\Phi = exp(\Delta G/k_B T) + 1$ and the cost of a pathway is the sum of the costs of the elementary steps involved. We further remove CRN products that are open-shell, as we generally believe that radical species should be short-lived. The CRN products vary depending on the initial conditions. A description of all predicted CRN products can be found in the Supporting Information (see Figures S14-S16).

Discovery of Elementary Reaction Mechanisms

We identified elementary reaction mechanisms using the AutoTS workflow,[52] which is powered by the Jaguar electronic structure code.[53] All initial transition-state searches were conducted using the ωB97X-D density functional with the def2-SVPD(-f) basis set and the PCM implicit solvent model with water as a solvent. A single-point energy correction was then applied using the ωB97M-V functional[54] with a larger def2-TZVPD basis set and the PCM implicit solvent model. We note that ωB97M-V is exceptionally accurate for calculations of reaction energy barriers and reaction thermodynamics.[55] All transition-states were validated by confirming that they connect the expected reaction endpoints. All energy barriers reported in this work are based on an infinite-separation approximation; that is, the free energies of reaction reactants and products are calculated from the free energies of individual isolated species, rather than reaction entrance or exit complexes.

Calculation of Reduction Potentials

When constructing and analyzing CRNs, we intentionally remove clusters with multiple molecules bound to Mg ions (see Species Filtering above). In part, this is necessary in order to limit the size of the CRN. However, this means that essentially all Mg ions in our dataset are undercoordinated. As we note (see Solvation Correction), for chemical reactions, we can account for this undercoordination via a simple linear correction to the free energy, but the same correction cannot easily be applied to reduction reactions, especially if Mg ions are being reduced.

Here we report reduction potentials based on calculations in implicit solvent at the ωB97X-D/def2-SVPD(-f)/PCM//ωB97M-V/def2-TZVPD/PCM level of theory. From the Gibbs free energies of the reduced and non-reduced species, the reduction potential is calculated as

$$E^{\circ}(V) = -(G_{reduced} - G_{non-reduced}) - 2.08 \tag{1}$$

where the Gibbs free energies are reported in eV and the shift by 2.08 V is necessary in order to report potentials referenced to a Mg/Mg^{2+} electrode. In the Supporting Information (Table S1), we also calculate reduction potentials where Mg ions are fully solvated by an explicit solvent shell.

Estimation of Solubility in Diglyme

We calculate the liquid-vapor solubility limits of CRN products in G2 S_{G2} via

$$S_{G2} = \frac{VP}{P_0} exp[\frac{-\Delta G_{solv}}{RT}] \tag{2}$$

where VP is the vapor pressure of the solute (in atmospheres or atm), P_0 is the pressure of a standard-state (1M) ideal gas at room temperature (24.45 atm), R is the ideal gas constant (8.314 J mol^{-1} K^{-1}), T is the absolute temperature (298.15 K for room temperature), and

ΔG_{solv} is the free energy of solvation. This equation assumes that the solutes of interest behave ideally in both the gas and the solution phase. We also neglect the effect of the dissolved salt in G2 and treat the solvent as a pure organic liquid. We predict the vapor pressure of CRN products using the SIMPOL[56] group contribution method (as implemented in UManSysProp),[57] and we calculate the free energy of solvation using SMD (specifically, via DFT calculations at the ωB97X-V/def2-TZVPPD/SMD(G2) level of theory). Because SIMPOL is specifically designed for multifunctional organic compounds, we instead provide experimental vapor pressures at room temperature for H_2 and H_2O.

We note that *ab initio* prediction of gas solubility limits is deeply challenging and an area of ongoing research. The method employed here was chosen for its ease and simplicity, rather than for its accuracy. While we believe it is sufficiently accurate to distinguish between species which should or should not evolve as gases from an electrolyte, we do not expect quantitatively accurate predictions of solubility limits.

Experimental Methods

Electrolyte Preparation

All reagents and solvents were prepared using a Schlenk line or glovebox (with < 1 ppm of O_2 and < 1 ppm H_2O) under an argon atmosphere. $Mg(TFSI)_2$ (99.5%, Solvionic) was dried under vacuum at 170 °C for 24 - 48 hours prior to use. G2 (anhydrous, 99%, Sigma-Aldrich) was distilled over calcium hydride and stored on 3 Å and 4 Å molecular sieves. The distilled G2 had a water content of < 5 ppm H_2O as measured by a Karl-Fischer Coulometer Titrator. $Mg(TFSI)_2$/G2 solutions were prepared in a glovebox with a volumetric flask charged with the appropriate amount of pre-dried $Mg(TFSI)_2$ powder dissolved in distilled G2 solvent.

Online Electrochemical Mass Spectrometry

Device Configuration

Online electrochemical mass spectrometry (OEMS), one category of the differential electrochemical mass spectrometry (DEMS), was used for the instaneous and quantitative analysis of the gaseous species generated during electrochemical experiments. A schematic of our OEMS experimental setup is provided in the Supporting Information (Figure S1).

In our work, a modified capillary OEMS was used, which consisted of a supporting inert gas as a flow carrier (He) and capillary inlet for mass spectroscopy. It has a moderate response time of 16s, and the flow rate was controlled at $\sim$ 20 μL/min by a flow meter. Other features in our OEMS include: 1) the ability to evacuate and flush the system with He after the DEMS cell was assembled inside the glovebox; 2) calibration to quantify the gaseous generation amount in real-time; and 3) flow system to enable detection of a small amount of gas production.

An FMA-2600/FVL-2600 SERIES Mass and Volumetric from OMEGA was used to control the flow rate of a He tank. The Hiden HPR-40 DEMS system was equipped with a quadrupole mass spectrometer and a QIC UF microflow capillary inlet (type 303452) with a flow rate of 12 µL/min. A PX409-015GUSBH (Pressure Sensor, 15 psi, Digital, Gauge, 1/16") transducer was used to measure the real-time pressure in order to quantify gaseous species. A total of five manual Swagelok ball valves (SS-41GS1) were incorporated into the system to allow evacuation of the gas line and control of the flow rate/testing. An ECC-DEMS cell from El-cell was used.

Electrochemical Measurements

A two-electrode setup was used for the experiments, with polished Mg metal as the Counter Electrode (CE) and reference electrode (RE) and a gold disc (Φ = 8 mm, Au, Aldrich, 99.99%, 0.1 mm thick) as the Working Electrode (WE).

OEMS Calibration

A calibration and conversion is required in order to report OEMS measured intensities in terms of either partial pressure or molar flow. The relative signal intensity of a species with mass-to-charge ratio M/Z ($x_{M/Z}$) is calculated as

$$x_{M/Z} = S_{M/Z}\frac{I_{M/Z} - B_{M/Z}}{I_{total}} \tag{3}$$

where $S_{M/Z}$ is a machine-specific sensitivity factor, $B_{M/Z}$ is the background intensity, $I_{M/Z}$ is the measured intensity at the mass-to-charge ratio of interest, and I_{total} is the total measured intensity.

Using the cell pressure P_{total}, the relative signal intensity $x_{M/Z}$ can be converted to a partial pressure

$$P_{M/Z} = P_{total}x_{M/Z} \tag{4}$$

From there, the quantity of gas detected (in mols) can be obtained using the ideal gas law:

$$n_{M/Z} = \frac{P_{M/Z}V}{RT} \tag{5}$$

where R is the ideal gas constant, T is the absolute gas in Kelvin, and V is the head space volume in the DEMS cell.

X-Ray Photoelectron Spectroscopy and Scanning Electron Microscopy

Mg cycling and deposition for ex-situ analyses were performed on planar Pt (111) textured substrates in a custom-built Teflon cell containing a Mg rod CE, Mg wire RE, and a WE area of 0.2 cm^2. These substrates were prepared by evaporation of the noble metal onto Ti-coated Si wafers and were cleaned prior to use with acetone, 3:1 H_2SO_4:H_2O_2 (piranha solution), and deionized water, successively. Deposited Mg films were successively rinsed in G2 and 1,2-dimethoxyethane. Samples were transferred for X-ray photoelectron spectroscopy (XPS)

using an inert transfer capsule. XPS was performed on a Kratos Axis Ultra spectrometer using a monochromatic Al K-α source. Analyses were performed on films after 10s Ar^+ sputtering, and quantification was performed using CasaXPS software. SEM was performed on a FEI Magellan microscope.

Results and Discussion

OEMS

A 0.5M $Mg(TFSI)_2$/G2 electrolyte was used to plate Mg onto Au at a cell voltage of -1.0 V for approximately four hours in the OEMS system described above. The electrochemical and OEMS measurements are shown in Figure 1; cyclic voltammetry data is shown in Supporting Information Figure S2. The current density during the potentiostatic hold (Figure 1a) is initially high (-2.65 mA/cm^2) but gradually decreases in magnitude over time as a result of increased resistance caused by electrode passivation. The dynamic resistance of the electrode interfaces is also evident from the sudden changes in current which occur at varying intervals.

The OEMS signal over the course of the experiment was integrated in order to identify the major peaks (Figure 1b; snapshot OEMS spectra are presented in Supporting Information Figures S3-S7). We ignore peaks at M/Z = 2, 4, 20, and 40, as these correspond to the carrier gas (He, M/Z = 2, 4) or Ar (M/Z = 20, 40) that was trapped in the $Mg(TFSI)_2$/G2 electrolyte after the electrolyte was distilled and the DEMS cell was assembled in an Ar-filled glovebox. Other major peaks include those at M/Z = 18, 28, 32, 36, and 45.

From the time-resolved measurements (Figure 1c), we find that the signal at M/Z = 18 is relatively stable after an initial increase, while the signal at M/Z = 28, 32, and 36 all reach a maximum at $\sim$ 1 hour and afterwards gradually decrease. In contrast (Figure 1d), the M/Z = 45 flow rapidly decays to a near-zero signal in the first few minutes of the experiment.

This initial difference in signal over time suggests that the species detected at M/Z = 18, 28, 32, and 36 are products of ongoing reactivity, while the species detected at M/Z =

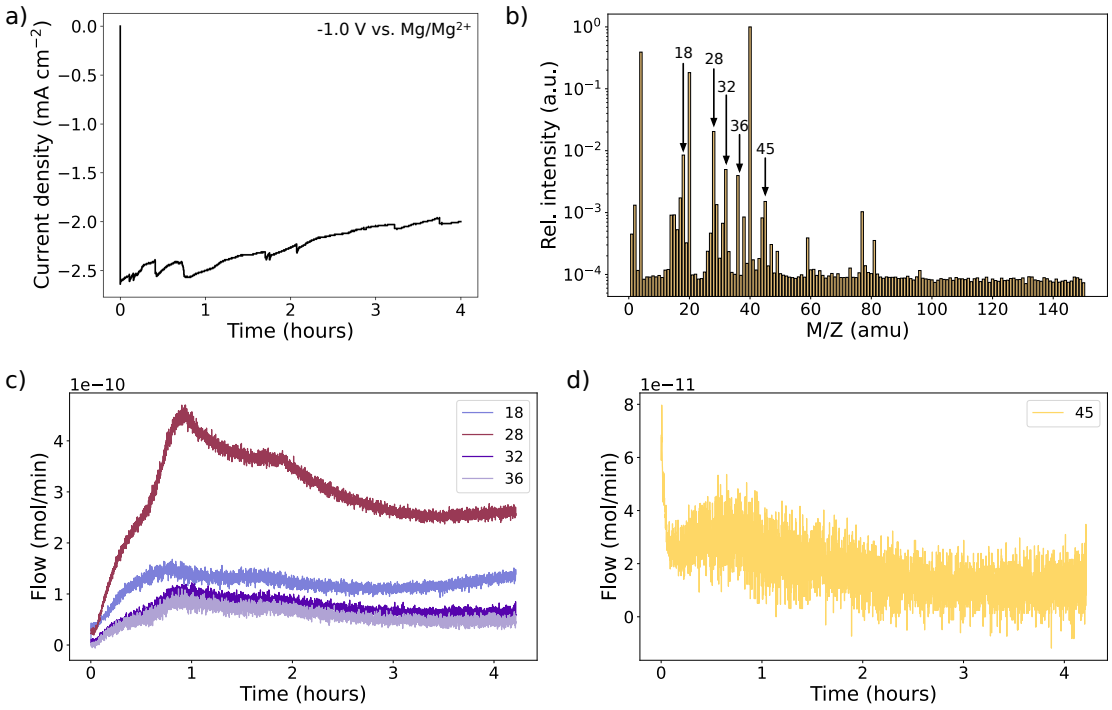

Figure 1: OEMS measurements on a $Mg(TFSI)_2$/G2 electrolyte during a potentiostatic hold at -1.0 V. a) The applied current density during potentiostatic hold; b) integrated relative OEMS intensity (in log scale) after approximately four hours of measurement, with major peaks indicated; c) time-resolved flow for several major peaks (M/Z = 18, 28, 32, 36) demonstrating continuous evolution; d) time-resolved flow for M/Z = 45 with initially high partial pressure that rapidly decays.

45 is either a decomposition product that can only form under highly specific conditions or is not indicative of a decomposition product at all. Given that this OEMS experiment was conducted in a constant-potential regime in which Mg is consistently plated (see Supporting Information Figure S2 for evidence of plating), we believe that the latter possibility is more likely. We suggest that the M/Z = 45 signal is likely indicative of G2 itself, rather than a product of G2 decomposition formed at the Mg electrode. The initially high M/Z = 45 signal reflects evaporated G2 that built up in the DEMS cell during preparation; after this initial G2 is purged, evaporation continues slowly, resulting in a lower signal during the remainder of the experiment. We note that OEMS is typically not sufficiently specific to allow positive identification of specific gases or molecular fragments. M/Z = 28, for instance, could indicate diatomic nitrogen (N_2, M = 28 amu), carbon monoxide (CO, M = 28 amu), or ethylene (C_2H_4, M = 28 amu), among other possibilities.

Identification of observed gases

In order to predict the identity of the major observed species, we constructed a CRN containing species that could be relevant to the decomposition of $Mg(TFSI)_2$/G2 electrolytes and subsequent interphase formation. Using stochastic simulations under five different initial conditions (see Identification of CRN Products), we identified 85 of an initial 6,469 species as CRN products (see Supporting Information for more discussion). We believe that most electrolyte decomposition products will either precipitate and contribute to an interphase layer, or else will be soluble in the electrolyte. Therefore, we filtered the predicted CRN products by their predicted solubility in G2 (S_{G2}), using Equation 2. Expecting considerable error in the prediction of S_{G2}, we remove any predicted CRN product with a predicted solubility > 5M. We also remove ionic CRN products and CRN products containing Mg, as we expect such species to be considerably more stable in solution than in the gas phase.

With these criteria, we predict that 14 of the 85 CRN products could evolve out of solution and be detected by OEMS (Figure 2). These predicted gaseous CRN products

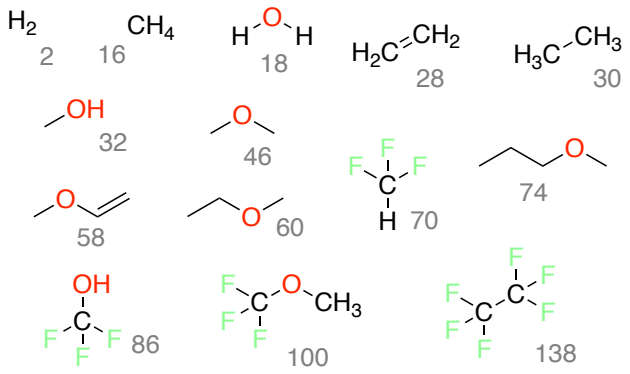

Figure 2: Gases predicted to evolve from $Mg(TFSI)_2$/G2 electrolytes, based on CRN analysis and prediction of solubility S_{G2}. The mass of each CRN product (rounded, in amu) is shown next to the 2D structure in gray.

enable the unambiguous assignment of the major observed OEMS peaks. For most peaks, there is exactly one gas that would be consistent with the signal. Specifically, the M/Z = 18 signal can be assigned to water (H_2O), the M/Z = 28 peak can be assigned to ethylene (C_2H_4), and the M/Z = 32 peak can be assigned to methanol (CH_3OH).

Notably, there are no predicted gaseous CRN products with masses consistent with M/Z = 36 and M/Z = 45 (though several species could produce fragments with M = 45 amu). This supports our previous suggestion that the M/Z = 45 signal does not correspond to a decomposition product but instead comes from another source such as evaporated G2. We further suggest that the M/Z = 36 signal corresponds to an impurity species, rather than a decomposition product of either G2 or $TFSI^-$. Considering that chloride (Cl^-) is an impurity in commercial $Mg(TFSI)_2$,[58] we tentatively assign the M/Z = 36 peak to hydrogen chloride (HCl). This assignment is also consistent with the presence of a minor M/Z = 38 signal. The ratio of the integrated M/Z = 36 signal and the M/Z = 38 signal is 4.67, which is close to the ratio of the natural abundances of ^{35}Cl to ^{37}Cl (3.17).[59]

Validating predicted major products

To confirm that the peak assignments based on CRN products are reasonable, we identified formation pathways to several CRN products using the previously constructed CRNs and

then used DFT to construct elementary reaction mechanisms.

There are several plausible pathways that lead to the formation of C_2H_4 (Figure 3a). All identified pathways initialize with Mg^{2+} being partially reduced in the presence of G2 ($M_1 \longrightarrow M_2$). It has previously been reported that the partial reduction of Mg^{2+} ions to highly reactive radical Mg^{1+} can promote electrolyte decomposition.[25,27] We predict that this reduction can occur at 0.64 V vs. Mg/Mg^{2+}; however, this and all other reported reduction potentials with Mg ions present depend on the solvation environment of the metal ion (see Supporting Information). Seguin et al.[27] previously showed that the partially reduced complex M_2 can cleave either of the internal C-O bonds with $\Delta G^{\ddagger} = 0.42$ eV due to a bifurcation of the potential energy surface. If a methoxide ion (CH_3O^-, M_3) is eliminated, we find that the remaining Mg-coordinated fragment (M_4) can subsequently reduce ($E^{\circ} = 3.51$ V) and eliminate C_2H_4 with a low barrier $\Delta G^{\ddagger} = 0.15$ eV. Alternatively, a radical $CH_3OCH_2CH_2^{\bullet}$ (M_6) can be eliminated. $CH_3OCH_2CH_2^{\bullet}$ can then coordinate with an additional Mg^{2+} and reduce ($M_6 \longrightarrow M_8$, $E^{\circ} = 3.89$ V), producing C_2H_4 with another low barrier ($\Delta G^{\ddagger} = 0.27$ eV). Though this latter mechanism involving $CH_3OCH_2CH_2^{\bullet}$ is more difficult, we nonetheless believe that it could occur, given that $M_3 + M_4$ and $M_5 + M_6$ are essentially equally likely to form from the initial cleavage of C-O bonds in G2.

If methoxide is present, for instance because of the mechanisms reported in Figure 3a, then the formation of methanol is facile and straightforward (Figure 3b). M_3 can attack either methylene group in Mg-coordinated G2 (M_1), abstracting a proton to form methanol ($M_3 + M_1 \longrightarrow M_{11} + M_{12}$, $\Delta G^{\ddagger} = 0.46$ eV; $M_3 + M_1 \longrightarrow M_{11} + M_{13}$, $\Delta G^{\ddagger} = 0.22$ eV). The deprotonated Mg-coordinated G2 species (M12, M13) are reactive and can further decompose. M12 can form M14, methoxyethene, ($M_{12} \longrightarrow M_5 + M_{14}$, $\Delta G^{\ddagger} = 0.25$ eV). While we predict M14 to be a potential gaseous product (Figure 2), we do not find evidence for significant methoxyethene evolution, perhaps because the deprotonation leading to M_{12} is slower than that leading to M_{13}. The decomposition of M_{13} instead produces magnesium methoxide ($M_{13} \longrightarrow M_{10} + M_{15}$, $\Delta G^{\ddagger} = 0.26$ eV), which could generate further methanol

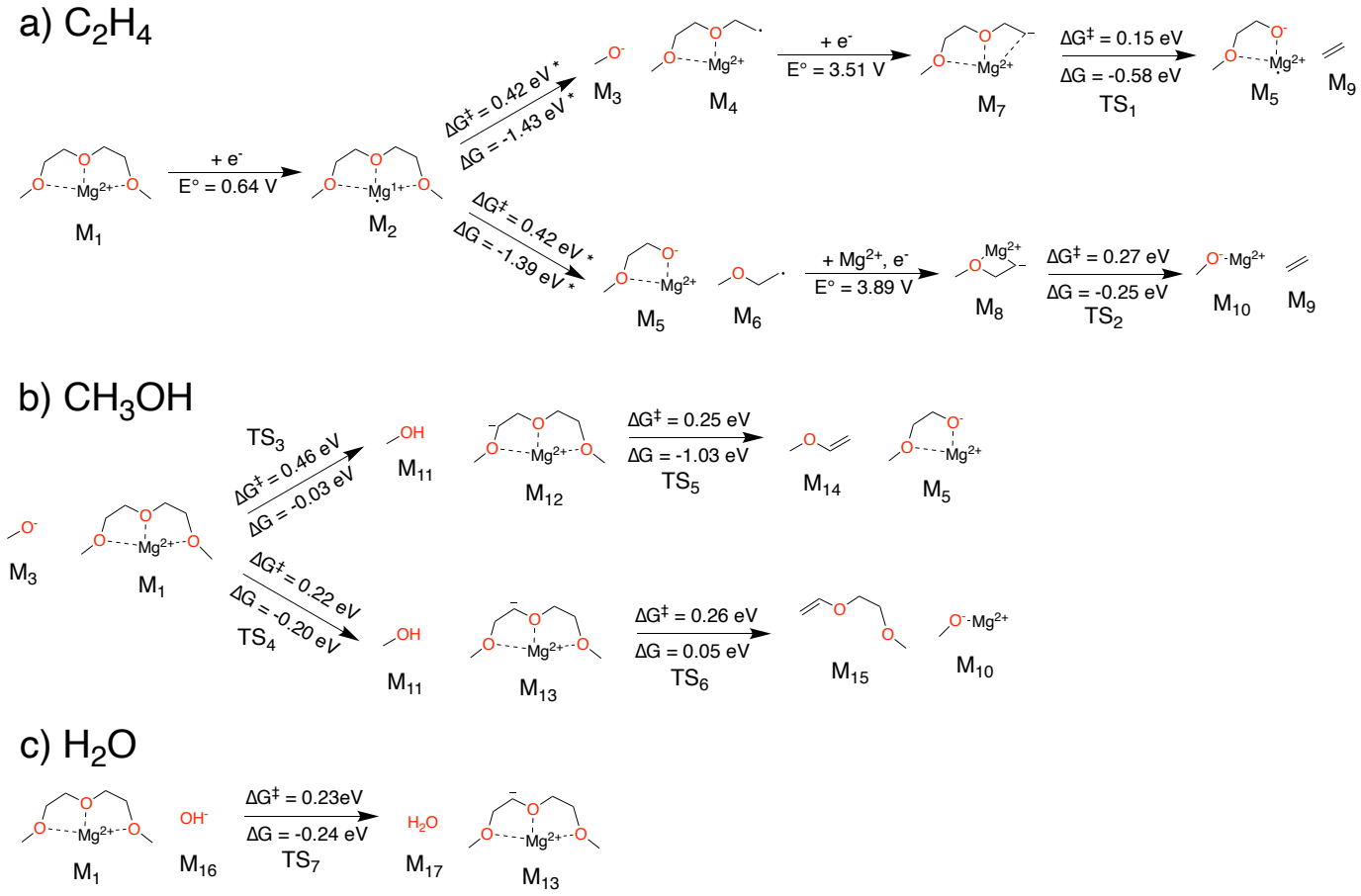

Figure 3: Elementary reaction mechanisms for the formation of a) C_2H_4, b) CH_3OH, and c) H_2O. Reaction energies and energy barriers marked with an asterisk (*) were taken from Seguin et al.[27]

by the mechanism just described. This suggests that methanol formation in G2 electrolytes may be autocatalytic; once methoxide is initially formed, it can be continually reformed via chemical reactions with G2.

Hydroxide ions can react with Mg-coordinated G2 similarly to methoxide, abstracting a proton to form water ($M_1 + M_{16} \longrightarrow M_{13} + M_{17}$, $\Delta G^{\ddagger} = 0.23$ eV). We note that this hydroxide could be free in the electrolyte solution (due to trace water) or could be present in the form of $Mg(OH)_2$, which should be expected on Mg electrodes. Hydroxide could also potentially arise from the reduction and decomposition of CH_3OH. The finding that G2, upon chelating Mg, can be deprotonated by hydroxide is in agreement with the prior work of Yu et al.[21] We note that the reduction potential of water is >1.5 V vs. Mg/Mg^{2+},[60] hence we expect that during charging of an MIB, water should quickly reform hydroxide, creating yet another potential autocatalytic loop.

Explaining absent gases

While several of the gases predicted to form via CRN analysis appear to be likely major products of G2 decomposition — namely, C_2H_4, CH_3OH, and H_2O — many of the predicted gaseous CRN products are not observed by OEMS. Just as we have used elementary reaction mechanism analysis to validate our spectroscopic peak assignment, indicating pathways that could reasonably lead to the identified gaseous CRN products, we can also suggest mechanistic explanations for why other gases are not evolved. Here, we consider three gases that were not observed experimentally in significant quantities: methane (CH_4), ethane (C_2H_6), and dimethyl ether (CH_3OCH_3).

Reaction mechanisms leading to CH_4 are shown in Figure 4a. Seguin et al. previously predicted that a methyl radical ($CH_3^{\bullet}$, M_{18}) could be eliminated from M_2 with a moderate barrier ($\Delta G^{\ddagger} = 0.67$ eV).[27] This reaction is accessible at room temperature but is several orders of magnitude slower than the other C-O cleavage reactions discussed previously (e.g. $M_2 \longrightarrow M_3 + M_4$). Even once M_{18} forms, the abstraction of H to form CH_4 is difficult.

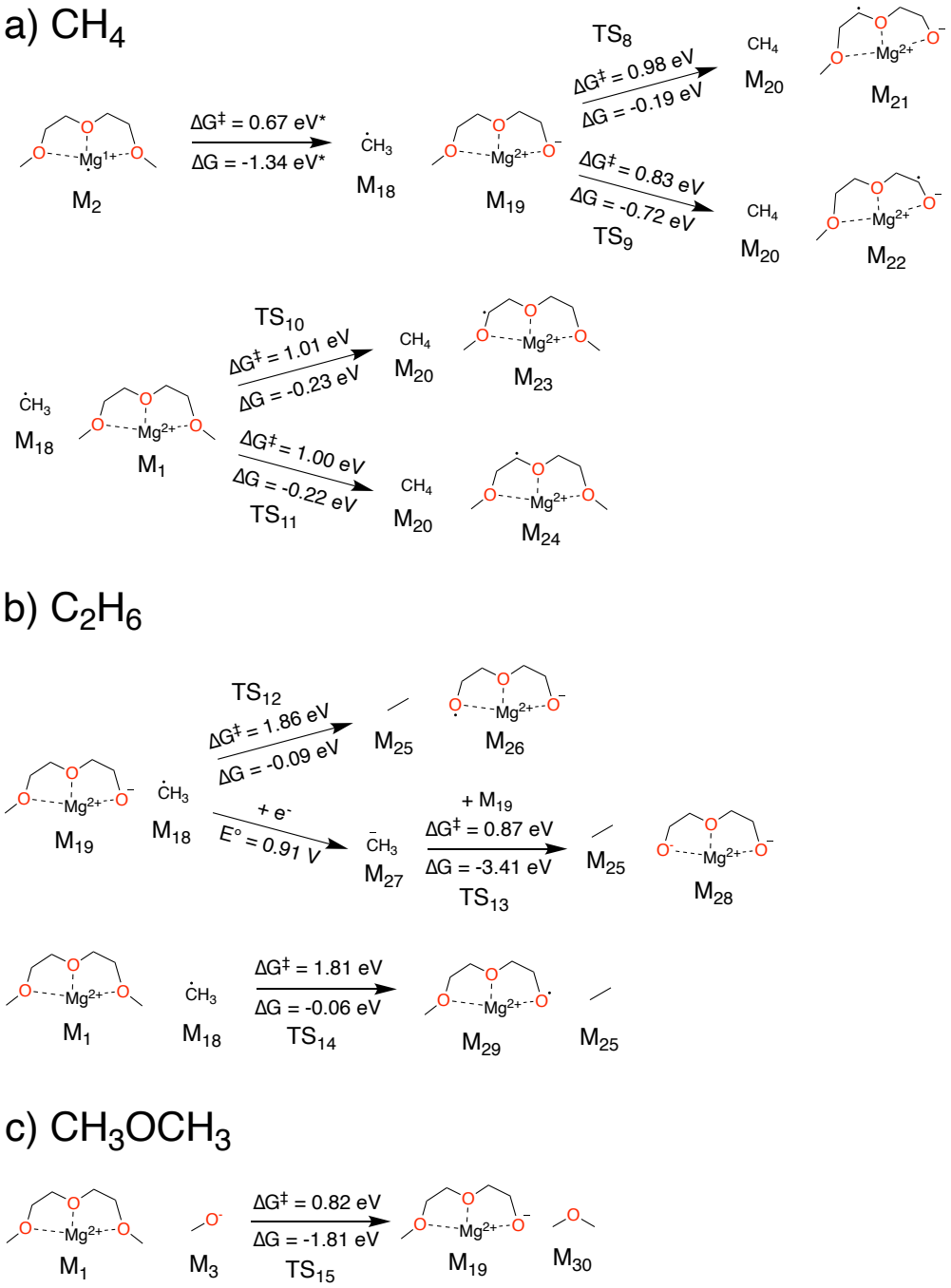

Figure 4: Elementary reaction mechanisms for the formation of a) CH_4, b) C_2H_6, and c) CH_3OCH_3. Reaction energies and energy barriers marked with an asterisk (*) were taken from Seguin et al.[27]

We have identified four different H abstraction reactions involving either Mg-coordinated G2 (M_1) or a reduced and partially decomposed Mg-coordinated G2 (M_{19}). The most facile abstraction ($M_{18} + M_{19} \longrightarrow M_{20} + M_{22}$) has a barrier of 0.83 eV; all others have barriers of $\sim$1 eV.

The formation of ethane (Figure 4b) is also kinetically limited. Like CH_4, C_2H_6 requires methyl radicals via the reaction $M_2 \longrightarrow M_{18} + M_{19}$. M_{18} could directly attack either M_{19} or M_1, transferring another methyl group to form C_2H_6. However, these reactions suffer from extremely high barriers $\sim$ 1.8 eV, and we therefore do not believe that they will occur under normal battery cycling conditions. If the methyl group reduces (E° = 0.91 V vs. Mg/Mg^{2+}) to form a methanide anion (M_{27}, CH_3^-), a similar methyl transfer reaction can occur ($M_{27} \longrightarrow M_{25} + M_{28}$); while this reaction is considerably more facile than those involving M_{18}, it is still sluggish at room temperature, with $\Delta G^\ddagger = 0.87$ eV. DFT is known to exhibit deficiencies in the prediction of energy barriers for radical-radical reactions, which is why we did not consider the reaction $CH_3^\bullet + CH_3^\bullet \longrightarrow C_2H_6$ (or $M_{18} + M_{18} \longrightarrow M_{25}$). Intuitively we believe that this reaction has a low barrier or is perhaps even barrierless. However, it would require two methyl radicals to form separately in close proximity, which seems unlikely considering that the decomposition of G2 to form $CH_3^\bullet$ is not preferred.

We find that dimethyl ether can form via methoxide (Figure 4c). The methoxide ion can attack a Mg-coordinated G2 in a single step ($M_1 + M_3 \longrightarrow M_{19} + M_{30}$, $\Delta G^\ddagger = 0.82$ eV). Because the formation of methanol by proton abstraction (e.g. $M_1 + M_3 \longrightarrow M_{11} + M_{13}$) is considerably more facile, dimethyl ether should not be expected to form, or should form only as a minority product.

The role of $TFSI^-$

Bistriflimide anions are known from both theoretical and experimental studies to be reductively unstable under MIB charging conditions.[22,23,25,61] It might therefore be expected that some fragments of $TFSI^-$ will be involved in gas evolution. Indeed, of the 14 potential

gaseous products shown in Figure 2, four of them contain trifluoromethyl groups ($-CF_3$) derived from $TFSI^-$. Trifluoromethyl groups in $TFSI^-$ can easily be eliminated under reducing conditions,[25] making it reasonable to think that CF_3 might react to form various small molecules. However, none of the major gases identified in OEMS contain $-CF_3$ or any other structural motif from bistriflimide. Moreover, none of the reaction mechanisms to form C_2H_4, CH_3OH, or H_2O require $TFSI^-$ or any related fragment. It appears that $TFSI^-$ is not involved in forming any evolved gases, in spite of its observed reactivity.

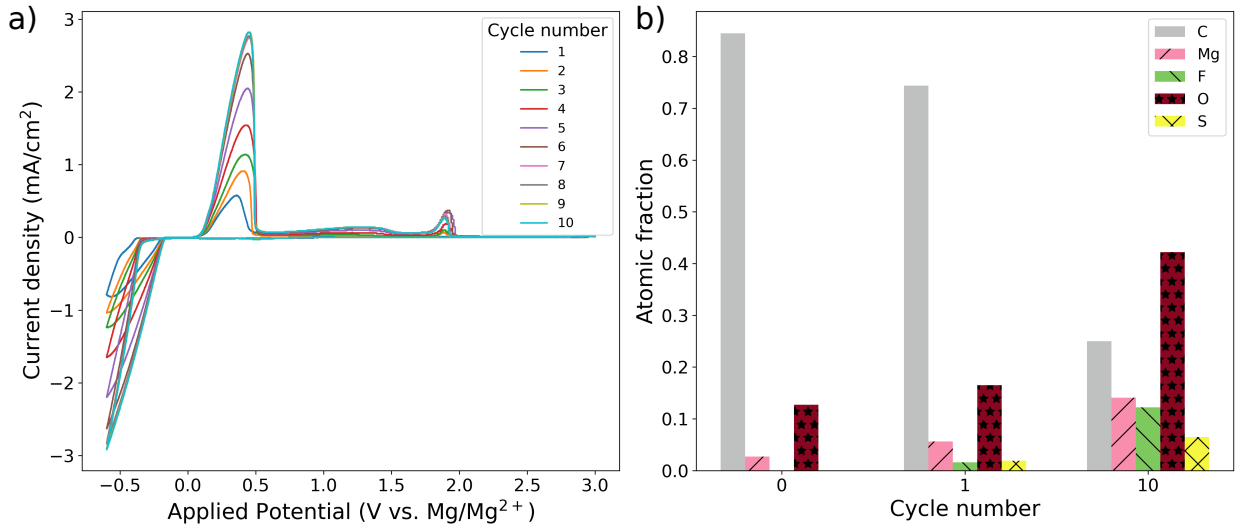

Figure 5: a) Progressive cyclic voltammetry cycling behavior (10 cycles) on a fresh Pt electrode in electrochemically conditioned 0.3M $Mg(TFSI)_2$/G2 at a scan rate of 10 mV/s. b) XPS-derived composition of the Pt electrode surface as a function of cycle number. A cycle number of 0 indicates that the measurement was taken before any potential had been applied.

If bistriflimide is not forming gases or assisting in the decomposition of G2, it raises the question of what happens to the TFSI- decomposition fragments. Recent AIMD results from Agarwal et al.[28] suggest that $TFSI^-$ might catastrophically decompose and even atomize at Mg interfaces, particularly if coordinated with Mg^{2+}. The results of Agarwal, which are based on simulations in the presence of an idealized, completely clean Mg electrode surface (with highly undercoordinated and therefore reactive Mg), may not explain $TFSI^-$ reactivity in all cases, for instance if a robust SEI layer or even thin oxide layer is present to shield

the electrolyte from a Mg metal electrode. However, in our experiment, we continuously plate Mg metal, potentially exposing fresh interfaces that can react with the electrolyte. We suggest that $TFSI^-$ decomposes at this newly formed metal interface, forming primarily solid deposits, rather than small molecules and gases.

Surface analysis provides further evidence that $TFSI^-$ forms solid deposits on the metallic Mg surface. We cycled a 0.3M $Mg(TFSI)_2$/G2 electrolyte between -0.6V and 3.0 V vs. Mg/Mg^{2+} 10 times on a Pt WE (Figure 5a) to determine if accumulation of a reaction product occurs with Mg deposition. During cycling, we used XPS to analyze the elemental composition of the surface film on the electrode (Figure 5b). Before cycling, the surface film was primarily composed of carbon (84.5%), with some oxygen (12.7%) and Mg (2.7%) and essentially no fluorine or sulfur. These results suggest that whereas G2 (containing C, O, and H, the latter of which cannot be detected by XPS) or G2 decomposition products from conditioning might be inherently unstable at a Pt surface, $TFSI^-$ (containing C, O, F, N, and S) is not inherently reactive. After the first cycle, some F (1.6%) and S (1.9%) are observed, indicating that $TFSI^-$ reacts electrochemically and that the products of $TFSI^-$ decomposition deposit on the electrode surface. The extent of $TFSI^-$ decomposition increases upon cycling, and by the 10th cycle, the surface film is 12.2% F and 6.5% S indicating accumulation of $TFSI^-$ reaction products. Notably, the atomic fraction of Mg in the surface film also increases with cycling, reflecting a degree of passivation-induced Mg stranding (Figure S17) as well as a loss of Mg inventory and battery capacity during cycling.

In addition to precipitated solid species, there is some evidence that $TFSI^-$ decomposition could result in products which are soluble in G2. A recent study on the effect of impurities in MIBs with glyme solvents by Yang et al.[62] applied electrospray ionization mass spectroscopy (ESI-MS) to study electrolyte speciation. The authors observed several F- and N-containing species in the electrolyte; because these were seen only in the conditioned electrolytes, these species could only come from $TFSI^-$ decomposition.

Conclusion

In this work, we used OEMS, CRNs, and DFT to identify gaseous byproducts of electrolyte decomposition in MIBs. From a CRN of over 6,000 species, we identified 14 possible gaseous species which could form from $Mg(TFSI)_2$/G2 electrolytes. Of these, three (C_2H_4, CH_3OH, and H_2O) were consistent with major peaks in the observed OEMS spectra. We validated our peak assignments by identifying elementary reaction mechanisms to these three species, finding in all cases that the species could be easily formed via Mg-coordinated G2 (and, in the case of H_2O, hydroxide ions). On the basis of reactive competition, we rationalized why other gases (CH_4, C_2H_6, and CH_3OCH_3) which were predicted to form may not actually emerge during MIB cycling. Although $TFSI^-$ decomposes at Mg metal electrodes and during Mg plating, we find that $TFSI^-$ does not itself form any gaseous species, nor is it necessary to assist in the decomposition of G2. Rather, we suggest that $TFSI^-$ primarily forms solid deposits on the electrode and potentially forms some products that are soluble in G2.

The methodology described here enables facile, in-depth analysis of *in situ* spectroscopy in electrochemical systems via powerful computational tools. While we have here focused on a model system in order to compare our results with previous experimental and theoretical findings, we believe that an approach mixing first-principles simulations, CRN exploration, and spectroscopy is especially well suited to allow for the characterization of completely novel electrolytes in which nothing is known regarding reactivity, decomposition products, and SEI formation. DEMS is a highly attractive point of comparison due to its high resolution, but CRN-assisted analysis of other spectroscopic measurements, such as infrared and nuclear magnetic resonance spectroscopies, should also be considered.

Author Contributions

Evan Walter Clark Spotte-Smith: Conceptualization, Data Curation, Formal Analysis, Funding Acquisition, Investigation, Methodology, Validation, Visualization, Writing — Original

Draft, Writing — Review & Editing; Samuel M. Blau: Conceptualization, Formal Analysis, Funding Acquisition, Investigation, Methodology, Supervision, Writing — Review & Editing; Daniel Barter: Formal Analysis, Investigation, Methodology, Software; Noel J. Leon: Investigation, Validation, Writing — Review & Editing; Nathan T. Hahn: Formal Analysis, Investigation, Methodology, Validation, Writing — Original Draft, Writing — Review & Editing; Nikita S. Redkar: Formal Analysis, Investigation, Writing — Review & Editing; Kevin R. Zavadil: Formal Analysis, Funding Acquisition, Investigation, Methodology, Supervision, Validation, Writing — Original Draft, Writing — Review & Editing; Chen Liao: Conceptualization, Formal Analysis, Funding Acquisition, Investigation, Methodology, Resources, Validation, Visualization, Writing — Original Draft, Writing — Review & Editing; Kristin A. Persson: Conceptualization, Funding Acquisition, Project Administration, Resources, Supervision, Writing — Review & Editing.

Conflicts of interest

There are no conflicts to declare.

Data Availability

The computational data used in this study is publicly available in a Figshare repository (DOI: 10.6084/m9.figshare.22189810.v1). Two Javascript Object Notation (JSON) files are included in this repository. `madeira.json` includes the properties (including structural, electronic, bonding, vibrational, and thermodynamic properties) of the 11,502 species in the MADEIRA dataset. `pathway_data.json` includes a more limited set of structural and thermodynamic properties calculated for all minima and transition-states reported in this work, labeled as they are in Figures 3 and 4.

Acknowledgements

This work is intellectually led the Joint Center for Energy Storage Research (JCESR), an Energy Innovation Hub funded by the U.S. Department of Energy, Office of Science, Basic Energy Sciences. Additional support is provided by the Kavli Energy NanoScience Institute Philomathia Graduate Student Fellowship (E.W.C.S.-S.), the Silicon Consortium Project directed by Brian Cunningham under the Assistant Secretary for Energy Efficiency and Renewable Energy, Office of Vehicle Technologies of the U.S. Department of Energy, Contract No. DE-AC02-05CH11231 (E.W.C.S.-S., K.A.P.), and the Laboratory Directed Research and Development Program of Lawrence Berkeley National Laboratory under U.S. Department of Energy Contract No. DE-AC02-05CH11231 (S.M.B., D.B.). Access to and assistance using the Schrödinger Suite of software tools, including Jaguar and AutoTS, was generously provided by Schrödinger, Inc. Data for this study was produced using computational resources provided by the National Energy Research Scientific Computing Center (NERSC), a U.S. Department of Energy Office of Science User Facility under Contract No. DE-AC02-05CH11231, the Eagle HPC system at the National Renewable Energy Laboratory (NREL), and the Lawrencium HPC cluster at Lawrence Berkeley National Laboratory.

Supporting Information

Schematic of experimental setup; cyclic voltammetry data; snapshot OEMS spectra; discussion of solvent corrections to free energy; discussion of predicted reduction potentials with and in the absence of explicit solvent; further description of CRN-predicted CRN products; average stochastic trajectories obtained during CRN analysis; SEM images.

References

(1) Ellis, L. D.; Badel, A. F.; Chiang, M. L.; Park, R. J.-Y.; Chiang, Y.-M. Toward electrochemical synthesis of cement—An electrolyzer-based process for decarbonating CaCO3 while producing useful gas streams. *Proceedings of the National Academy of Sciences* **2020**, *117*, 12584–12591.

(2) Woldu, A. R.; Huang, Z.; Zhao, P.; Hu, L.; Astruc, D. Electrochemical CO2 reduction (CO2RR) to multi-carbon products over copper-based catalysts. *Coordination Chemistry Reviews* **2022**, *454*, 214340.

(3) Tarpeh, W. A.; Barazesh, J. M.; Cath, T. Y.; Nelson, K. L. Electrochemical Stripping to Recover Nitrogen from Source-Separated Urine. *Environmental Science & Technology* **2018**, *52*, 1453–1460.

(4) Manzetti, S.; Mariasiu, F. Electric vehicle battery technologies: From present state to future systems. *Renewable and Sustainable Energy Reviews* **2015**, *51*, 1004–1012.

(5) Zhu, Z.; Jiang, T.; Ali, M.; Meng, Y.; Jin, Y.; Cui, Y.; Chen, W. Rechargeable Batteries for Grid Scale Energy Storage. *Chemical Reviews* **2022**, *122*, 16610–16751.

(6) Martinez Alvarado, J. I.; Meinhardt, J. M.; Lin, S. Working at the interfaces of data science and synthetic electrochemistry. *Tetrahedron Chem* **2022**, *1*, 100012.

(7) Zahrt, A. F.; Mo, Y.; Nandiwale, K. Y.; Shprints, R.; Heid, E.; Jensen, K. F. Machine-Learning-Guided Discovery of Electrochemical Reactions. *Journal of the American Chemical Society* **2022**, *144*, 22599–22610.

(8) Wang, L.; Menakath, A.; Han, F.; Wang, Y.; Zavalij, P. Y.; Gaskell, K. J.; Borodin, O.; Iuga, D.; Brown, S. P.; Wang, C.; Xu, K.; Eichhorn, B. W. Identifying the components of the solid–electrolyte interphase in Li-ion batteries. *Nature Chemistry* **2019**, *11*, 789–796.

(9) Lee, C. W.; Cho, N. H.; Im, S. W.; Jee, M. S.; Hwang, Y. J.; Min, B. K.; Nam, K. T. New challenges of electrokinetic studies in investigating the reaction mechanism of electrochemical CO2 reduction. *Journal of Materials Chemistry A* **2018**, *6*, 14043–14057.

(10) Plesniak, M. P.; Huang, H.-M.; Procter, D. J. Radical cascade reactions triggered by single electron transfer. *Nature Reviews Chemistry* **2017**, *1*, 1–16.

(11) Verma, P.; Maire, P.; Novák, P. A review of the features and analyses of the solid electrolyte interphase in Li-ion batteries. *Electrochimica Acta* **2010**, *55*, 6332–6341.

(12) An, S. J.; Li, J.; Daniel, C.; Mohanty, D.; Nagpure, S.; Wood, D. L. The state of understanding of the lithium-ion-battery graphite solid electrolyte interphase (SEI) and its relationship to formation cycling. *Carbon* **2016**, *105*, 52–76.

(13) Olivetti, E. A.; Ceder, G.; Gaustad, G. G.; Fu, X. Lithium-Ion Battery Supply Chain Considerations: Analysis of Potential Bottlenecks in Critical Metals. *Joule* **2017**, *1*, 229–243.

(14) Sun, X.; Hao, H.; Hartmann, P.; Liu, Z.; Zhao, F. Supply risks of lithium-ion battery materials: An entire supply chain estimation. *Materials Today Energy* **2019**, *14*, 100347.

(15) Brown, O. R.; McIntyre, R. The magnesium and magnesium amalgam electrodes in aprotic organic solvents a kinetic study. *Electrochimica Acta* **1985**, *30*, 627–633.

(16) Genders, J. D.; Pletcher, D. Studies using microelectrodes of the Mg(II)/Mg couple in tetrahydrofuran and propylene carbonate. *Journal of Electroanalytical Chemistry and Interfacial Electrochemistry* **1986**, *199*, 93–100.

(17) Aurbach, D.; Gofer, Y.; Lu, Z.; Schechter, A.; Chusid, O.; Gizbar, H.; Cohen, Y.; Ashkenazi, V.; Moshkovich, M.; Turgeman, R.; Levi, E. A short review on the com-

parison between Li battery systems and rechargeable magnesium battery technology. *Journal of Power Sources* **2001**, *97-98*, 28–32.

(18) Shterenberg, I.; Salama, M.; Yoo, H. D.; Gofer, Y.; Park, J.-B.; Sun, Y.-K.; Aurbach, D. Evaluation of (CF3SO2)2N (TFSI) Based Electrolyte Solutions for Mg Batteries. *Journal of The Electrochemical Society* **2015**, *162*, A7118.

(19) Arthur, T. S.; Glans, P.-A.; Singh, N.; Tutusaus, O.; Nie, K.; Liu, Y.-S.; Mizuno, F.; Guo, J.; Alsem, D. H.; Salmon, N. J.; Mohtadi, R. Interfacial Insight from Operando XAS/TEM for Magnesium Metal Deposition with Borohydride Electrolytes. *Chemistry of Materials* **2017**, *29*, 7183–7188.

(20) Gao, T.; Hou, S.; Huynh, K.; Wang, F.; Eidson, N.; Fan, X.; Han, F.; Luo, C.; Mao, M.; Li, X.; Wang, C. Existence of Solid Electrolyte Interphase in Mg Batteries: Mg/S Chemistry as an Example. *ACS Applied Materials & Interfaces* **2018**, *10*, 14767–14776.

(21) Yu, Y.; Baskin, A.; Valero-Vidal, C.; Hahn, N. T.; Liu, Q.; Zavadil, K. R.; Eichhorn, B. W.; Prendergast, D.; Crumlin, E. J. Instability at the Electrode/Electrolyte Interface Induced by Hard Cation Chelation and Nucleophilic Attack. *Chemistry of Materials* **2017**, *29*, 8504–8512.

(22) Yoo, H. D.; Han, S.-D.; Bolotin, I. L.; Nolis, G. M.; Bayliss, R. D.; Burrell, A. K.; Vaughey, J. T.; Cabana, J. Degradation Mechanisms of Magnesium Metal Anodes in Electrolytes Based on (CF3SO2)2N– at High Current Densities. *Langmuir* **2017**, *33*, 9398–9406.

(23) Jay, R.; Tomich, A. W.; Zhang, J.; Zhao, Y.; De Gorostiza, A.; Lavallo, V.; Guo, J. Comparative Study of Mg(CB11H12)2 and Mg(TFSI)2 at the Magnesium/Electrolyte Interface. *ACS Applied Materials & Interfaces* **2019**, *11*, 11414–11420.

(24) Nguyen, D.-T.; Eng, A. Y. S.; Ng, M.-F.; Kumar, V.; Sofer, Z.; Handoko, A. D.; Subra-

manian, G. S.; Seh, Z. W. A High-Performance Magnesium Triflate-based Electrolyte for Rechargeable Magnesium Batteries. *Cell Reports Physical Science* **2020**, *1*, 100265.

(25) Rajput, N. N.; Qu, X.; Sa, N.; Burrell, A. K.; Persson, K. A. The Coupling between Stability and Ion Pair Formation in Magnesium Electrolytes from First-Principles Quantum Mechanics and Classical Molecular Dynamics. *Journal of the American Chemical Society* **2015**, *137*, 3411–3420.

(26) Lowe, J. S.; Siegel, D. J. Reaction Pathways for Solvent Decomposition on Magnesium Anodes. *The Journal of Physical Chemistry C* **2018**, *122*, 10714–10724.

(27) Seguin, T. J.; Hahn, N. T.; Zavadil, K. R.; Persson, K. A. Elucidating Non-aqueous Solvent Stability and Associated Decomposition Mechanisms for Mg Energy Storage Applications From First-Principles. *Frontiers in Chemistry* **2019**, *7*, 175.

(28) Agarwal, G.; Howard, J. D.; Prabhakaran, V.; Johnson, G. E.; Murugesan, V.; Mueller, K. T.; Curtiss, L. A.; Assary, R. S. Insights into Spontaneous Solid Electrolyte Interphase Formation at Magnesium Metal Anode Surface from Ab Initio Molecular Dynamics Simulations. *ACS Applied Materials & Interfaces* **2021**, *13*, 38816–38825.

(29) Novák, P.; Panitz, J. C.; Joho, F.; Lanz, M.; Imhof, R.; Coluccia, M. Advanced in situ methods for the characterization of practical electrodes in lithium-ion batteries. *Journal of Power Sources* **2000**, *90*, 52–58.

(30) McCloskey, B. D.; Bethune, D. S.; Shelby, R. M.; Girishkumar, G.; Luntz, A. C. Solvents' Critical Role in Nonaqueous Lithium–Oxygen Battery Electrochemistry. *The Journal of Physical Chemistry Letters* **2011**, *2*, 1161–1166.

(31) Tsiouvaras, N.; Meini, S.; Buchberger, I.; Gasteiger, H. A. A Novel On-Line Mass Spectrometer Design for the Study of Multiple Charging Cycles of a Li-O2 Battery. *Journal of The Electrochemical Society* **2013**, *160*, A471.

(32) Nie, K.; Wang, X.; Qiu, J.; Wang, Y.; Yang, Q.; Xu, J.; Yu, X.; Li, H.; Huang, X.; Chen, L. Increasing Poly(ethylene oxide) Stability to 4.5 V by Surface Coating of the Cathode. *ACS Energy Letters* **2020**, *5*, 826–832.

(33) Shi, B.; Liu, K.; Lee, E.; Liao, C. *Batteries: Materials principles and characterization methods*; IOP Publishing, 2021; Chapter 5: Differential electrochemical mass spectrometry (DEMS) for batteries.

(34) Barter, D.; Spotte-Smith, E. W. C.; S. Redkar, N.; Khanwale, A.; Dwaraknath, S.; A. Persson, K.; M. Blau, S. Predictive stochastic analysis of massive filter-based electrochemical reaction networks. *Digital Discovery* **2023**, 123–137.

(35) Spotte-Smith, E. W. C.; Blau, S. M.; Xie, X.; Patel, H. D.; Wen, M.; Wood, B.; Dwaraknath, S.; Persson, K. A. Quantum chemical calculations of lithium-ion battery electrolyte and interphase species. *Scientific Data* **2021**, *8*, 203.

(36) Mardirossian, N.; Head-Gordon, M. B97X-V: A 10-parameter, range-separated hybrid, generalized gradient approximation density functional with nonlocal correlation, designed by a survival-of-the-fittest strategy. *Physical Chemistry Chemical Physics* **2014**, *16*, 9904–9924.

(37) Rappoport, D.; Furche, F. Property-optimized Gaussian basis sets for molecular response calculations. *The Journal of Chemical Physics* **2010**, *133*, 134105.

(38) Marenich, A. V.; Cramer, C. J.; Truhlar, D. G. Universal Solvation Model Based on Solute Electron Density and on a Continuum Model of the Solvent Defined by the Bulk Dielectric Constant and Atomic Surface Tensions. *The Journal of Physical Chemistry B* **2009**, *113*, 6378–6396.

(39) Qu, X.; Jain, A.; Rajput, N. N.; Cheng, L.; Zhang, Y.; Ong, S. P.; Brafman, M.; Maginn, E.; Curtiss, L. A.; Persson, K. A. The Electrolyte Genome project: A big data

approach in battery materials discovery. *Computational Materials Science* **2015**, *103*, 56–67.

(40) Epifanovsky, E. et al. Software for the frontiers of quantum chemistry: An overview of developments in the Q-Chem 5 package. *The Journal of Chemical Physics* **2021**, *155*, 084801.

(41) Mathew, K. et al. Atomate: A high-level interface to generate, execute, and analyze computational materials science workflows. *Computational Materials Science* **2017**, *139*, 140–152.

(42) Ong, S. P.; Richards, W. D.; Jain, A.; Hautier, G.; Kocher, M.; Cholia, S.; Gunter, D.; Chevrier, V. L.; Persson, K. A.; Ceder, G. Python Materials Genomics (pymatgen): A robust, open-source python library for materials analysis. *Computational Materials Science* **2013**, *68*, 314–319.

(43) Blau, S.; Spotte-Smith, E. W. C.; Wood, B.; Dwaraknath, S.; Persson, K. Accurate, Automated Density Functional Theory for Complex Molecules Using On-the-fly Error Correction. *ChemRxiv* **2020**, DOI:10.26434/chemrxiv.13076030.v1.

(44) Spotte-Smith, E. W. C.; Blau, S. M.; Barter, D.; Leon, N. J.; Hahn, N. T.; Redkar, N. S.; Zavadil, K. R.; Liao, C.; Persson, K. A. Data for "Chemical Reaction Networks Explain Gas Evolution Mechanisms in Mg-Ion Batteries". 2023; `https://doi.org/10.6084/m9.figshare.22189810.v1`.

(45) Chai, J.-D.; Head-Gordon, M. Long-range corrected hybrid density functionals with damped atom–atom dispersion corrections. *Physical Chemistry Chemical Physics* **2008**, *10*, 6615–6620.

(46) Klamt, A. The COSMO and COSMO-RS solvation models. *WIREs Computational Molecular Science* **2011**, *1*, 699–709.

(47) Weinhold, F.; Glendening, E. D. NBO 5.0 program manual: natural bond orbital analysis programs. *Theoretical Chemistry Institute and Department of Chemistry, University of Wisconsin, Madison, WI* **2001**, *53706*.

(48) Shang, C.; Liu, Z.-P. Stochastic Surface Walking Method for Structure Prediction and Pathway Searching. *Journal of Chemical Theory and Computation* **2013**, *9*, 1838–1845.

(49) Spotte-Smith, E. W. C.; Kam, R. L.; Barter, D.; Xie, X.; Hou, T.; Dwaraknath, S.; Blau, S. M.; Persson, K. A. Toward a Mechanistic Model of Solid–Electrolyte Interphase Formation and Evolution in Lithium-Ion Batteries. *ACS Energy Letters* **2022**, *7*, 1446–1453.

(50) Gillespie, D. T. Exact stochastic simulation of coupled chemical reactions. *The Journal of Physical Chemistry* **1977**, *81*, 2340–2361.

(51) Gillespie, D. T. Stochastic Simulation of Chemical Kinetics. *Annual Review of Physical Chemistry* **2007**, *58*, 35–55.

(52) Jacobson, L. D.; Bochevarov, A. D.; Watson, M. A.; Hughes, T. F.; Rinaldo, D.; Ehrlich, S.; Steinbrecher, T. B.; Vaitheeswaran, S.; Philipp, D. M.; Halls, M. D.; Friesner, R. A. Automated Transition State Search and Its Application to Diverse Types of Organic Reactions. *Journal of Chemical Theory and Computation* **2017**, *13*, 5780–5797.

(53) Bochevarov, A. D.; Harder, E.; Hughes, T. F.; Greenwood, J. R.; Braden, D. A.; Philipp, D. M.; Rinaldo, D.; Halls, M. D.; Zhang, J.; Friesner, R. A. Jaguar: A high-performance quantum chemistry software program with strengths in life and materials sciences. *International Journal of Quantum Chemistry* **2013**, *113*, 2110–2142.

(54) Mardirossian, N.; Head-Gordon, M. B97M-V: A combinatorially optimized, range-separated hybrid, meta-GGA density functional with VV10 nonlocal correlation. *The Journal of Chemical Physics* **2016**, *144*, 214110.

(55) Mardirossian, N.; Head-Gordon, M. Thirty years of density functional theory in computational chemistry: an overview and extensive assessment of 200 density functionals. *Molecular Physics* **2017**, *115*.

(56) Pankow, J. F.; Asher, W. E. SIMPOL.1: a simple group contribution method for predicting vapor pressures and enthalpies of vaporization of multifunctional organic compounds. *Atmospheric Chemistry and Physics* **2008**, *8*, 2773–2796.

(57) Topping, D.; Barley, M.; Bane, M. K.; Higham, N.; Aumont, B.; Dingle, N.; McFiggans, G. UManSysProp v1.0: an online and open-source facility for molecular property prediction and atmospheric aerosol calculations. *Geoscientific Model Development* **2016**, *9*, 899–914.

(58) Connell, J. G.; Genorio, B.; Lopes, P. P.; Strmcnik, D.; Stamenkovic, V. R.; Markovic, N. M. Tuning the Reversibility of Mg Anodes via Controlled Surface Passivation by H2O/Cl– in Organic Electrolytes. *Chemistry of Materials* **2016**, *28*, 8268–8277.

(59) Coplen, T. B.; Böhlke, J. K.; De Bievre, P.; Ding, T.; Holden, N.; Hopple, J.; Krouse, H.; Lamberty, A.; Peiser, H.; Revesz, K.; others, Isotope-abundance variations of selected elements (IUPAC Technical Report). *Pure and applied chemistry* **2002**, *74*, 1987–2017.

(60) Haynes, W.; Lide, D.; Bruno, T. *CRC handbook of chemistry and physics*; CRC Press, 2012.

(61) Baskin, A.; Prendergast, D. Exploration of the Detailed Conditions for Reductive Stability of Mg(TFSI)2 in Diglyme: Implications for Multivalent Electrolytes. *The Journal of Physical Chemistry C* **2016**, *120*, 3583–3594.

(62) Yang, Z.; Yang, M.; Hahn, N. T.; Connell, J.; Bloom, I.; Liao, C.; Ingram, B. J.; Trahey, L. Toward practical issues: Identification and mitigation of the impurity effect in glyme solvents on the reversibility of Mg plating/stripping in Mg batteries. *Frontiers in Chemistry* **2022**, *10*.